IEEE Access
Multidisciplinary | Rapid Review | Open Access Journal

Received January 5, 2021, accepted January 19, 2021, date of publication January 26, 2021, date of current version February 2, 2021.

Digital Object Identifier 10.1109/ACCESS.2021.3054773

Grid Voltage Sensorless Model Predictive Control for a Single-Phase T-Type Rectifier With an Active Power Decoupling Circuit

SERTAC BAYHAN, (Senior Member, IEEE)
Qatar Environment and Energy Research Institute, Hamad Bin Khalifa University, Doha 5825, Qatar
e-mail: sbayhan@hbku.edu.qa

This work was supported in part by the from the Qatar National Research Fund (a member of Qatar Foundation) under Grant NPRP12S-0214-190083, and in part by the Open Access funding provided by the Qatar National Library.

ABSTRACT This paper proposes grid voltage sensorless model predictive control for a single-phase T-type rectifier with an active power decoupling circuit. The proposed sensorless technique is based on a model reference adaptive system (MRAS) and tested under distorted grid conditions. This study also examines the relationship among the ripple energy, the dc-link capacitor, and the active power decoupling circuit capacitor. The developed control technique is proposed to ensure the following objectives; (1) sensorless grid voltage estimation; (2) the second-order ripple power elimination; (3) reference current generation based on power equilibrium; (4) ensuring unity power factor under all operating conditions; and (5) capacitor voltage balance. The developed control structure offers simplicity and it is cost-effective due to the absence of a grid voltage sensor. An experimental prototype is established, and the main results, including the steady-state and dynamic performances, are presented to validate the effectiveness of the proposed control.

INDEX TERMS Sensorless control, model predictive control, active power decoupling, single-phase PWM rectifiers.

I. INTRODUCTION

In the last few decades, there has been a dramatic increase in using pulse-width modulated (PWM) rectifiers in single-phase systems as they play a pivotal role in various applications e.g., battery chargers, uninterruptible power supply (UPS), and light-emitting-diodes (LED). Despite the single-phase PWM rectifier efficacy and better power quality profile, they suffer from the second-order (2ω) harmonic currents and corresponding ripple voltages on the dc-link, like other single-phase converters [1]. In the case of battery chargers, the 2ω harmonic current ripple flowing through batteries results in overheating and premature aging. Consequently, the single-phase rectifiers require a filtering solution so as to ensure a smooth dc-link voltage and current [2].

The filtering solutions can be classified into two main groups, namely passive and active filtering techniques [3]. The main idea of the passive solutions is to attach a large electrolytic capacitor on the dc-link, and the size of the capacitor depends on the pulsating power. Although this passive solution is simple and easy to implement, it has some problems in use. One of the most significant challenges is the electrolytic capacitors' short lifespan, which significantly has an impact on the mean time between failures of the rectifiers [4]. Furthermore, the large volume and weight of dc-link capacitors are undesirable from the cost and practicability perspective. A number of studies have considered the disadvantages of passive filtering techniques and these studies have proposed active filtering techniques as an alternative to passive solutions. The basic idea behind active techniques is based on an auxiliary circuit that diverts the pulsating power from the dc-link capacitor to another energy storage component such as capacitor or inductor. This auxiliary circuit eliminates the deficiency mentioned above by using film capacitors. On the other hand, active techniques require additional components (transistors, capacitors, and inductors) that may increase the system cost and complexity [5]. For that reason, the auxiliary circuit design and its control structure play an important role in meeting the requirements for volume and weight critical applications.

There is a large number of published studies suggesting active filtering techniques and their control structures [6].

The associate editor coordinating the review of this manuscript and approving it for publication was Yuh-Shyan Hwang.

The active power decoupling topologies can be divided into two main categories. In the first category, the main power converter (dc/ac or ac/dc) and active power decoupling circuit (auxiliary circuit) operate independently [7]. In the second category, however, the active power decoupling circuit shares some or all switches with the main power converter [8]. The control structure of the active power coupling circuit can either be open-loop or closed-loop. Although the open-loop control is easy to implement, this control structure is sensitive to the parameters change. For that reason, it is not robust against parameter variations. To overcome the weakness of open-loop control, a number of closed-loop control techniques have been proposed [9]. The proportional-integral (PI) or proportional-resonant (PR) regulators are widely used to ensure the active power decoupling circuit voltage and current tracking performance. However, the design of a stable closed-loop control algorithm is not straightforward.

The power converters in some specialized applications such as electric aircraft and electric-drive ships need to be designed to ensure high power density. Multilevel topologies bring considerable advantages in such system design over two-level counterparts for a smaller volume of passive filters, lower voltage stress on the semiconductor devices, lower common-mode voltage, and higher conversion efficiency [10]. The most established and commercialized multilevel topologies are neutral-point-clamped (NPC), T-type, and flying capacitor (FC) converters. The T-type multilevel converter is advantages over NPC and FC converters for lower switching losses, reduced component count, and increased efficiency. The T-type converter is usually preferred in low-voltage applications, especially when the efficiency and cost are critical factors for specific applications. Besides, there are no clamping diodes in the T-type converters that result in a smaller component count compared to the NPC converters [11]. To sum up, the T-type converter takes the benefits of low conduction and switching losses and low switching voltage stress. The T-type converter presents low conduction and switching losses as well as low voltage stress on the switches [12].

Traditionally, the control system of T-type single-phase PWM rectifier requires one grid voltage sensor, one line current sensor, and two voltage sensors for the dc-link capacitors [13]. These sensors are relatively expensive compared to the total cost of the control system and decrease the system reliability. More recent attention has focused on the provision of sensorless control of the PWM rectifiers to decrease the cost of the control system as well as reduce the required space for the hardware design. There is a large number of published studies that present the various sensorless control techniques, including estimating the grid voltages based on instantaneous power theory [14], sliding-mode technique [15], state observer methods [16], and virtual flux (VF) techniques [17]. The main disadvantage of these techniques is that they suffer from a substantial calculation burden. Model reference adaptive system (MRAS) observers are well known for sensorless control of induction machines and have many advantages compared to other estimation methods [18]. For that reason, the grid voltage sensorless technique employed in this study is based on MRAS. The MRAS based technique uses active and reactive power models to estimate grid voltage in this study.

To date, several studies have been proposed for T-type rectifier control [13], [19]. In [19], fault-tolerant control strategy for the T-type rectifier was presented in order to improve the reliability of the rectifier during an inner and outer open-switch fault. It was claimed that the proposed tolerant control technique was advantageous in the dynamic response. In [13], a sliding mode control approach was proposed in order to control the dc-link voltage of the three-phase T-type rectifier. The proposed approach requires a PI controller to generate line current references. Although the implementation is easy, using the PI controller in the control system causes a slow dynamic response, therefore other control techniques are required for further response improvement.

A model predictive control (MPC) approach has been accepted by many scientists as a powerful control technique for power electronic converters because of its excellent performance in terms of nonlinear control, multi-objective optimization, and dynamic response. The existing literature on MPC is extensive and focuses particularly on the control of power electronic converters in various systems, including motor control applications [20], photovoltaic (PV) applications [21], grid-connected inverter applications [22], [23], etc. Furthermore, the MPC based control technique is proposed to regulate the line current as well as the dc-link voltage of the single-phase NPC rectifier [24]. On the other hand, this study has suffered from a lack of clarity in defining the optimization problem, and it is not considering the effect of 2ω harmonic current ripple.

In this paper, MPC based control strategy is proposed for the single-phase T-type rectifier. The proposed control approach improves overall system performance and efficiency. Experimental investigations are conducted to verify the proposed system performance. The main contributions of this study are summarized as follows.

1) The reference current generation is based on energy equilibrium that eliminates the PI controller. Thus, the dynamic response of the controller is improved.
2) The power decoupling circuit is used for buffering 2ω ripple power. This reduces the overall system size and cost significantly.
3) The grid voltage is estimated by MRAS based sensorless observer. This feature increases the system reliability and reduces the overall controller cost and size.
4) The dc-link capacitors voltages are kept balanced through the developed MPC.
5) The robustness of the proposed controller against parameter mismatch is studied with parameter variations.
6) The designed system operates at unity power factor under all operating conditions.

The rest of this paper is organized as follows: various aspects of the single-phase T-type rectifier with the active power coupling circuit, including the topology, its operation, ripple energy analysis, and dc-link capacitor analysis, are detailed in Section II. Then, the proposed control structure is presented in Section III. After that, extensive experimental results are presented in Section IV, with conclusions made in Section V.

II. SYSTEM MODEL AND ANALYSIS

This section describes the operating principle and mathematical model of the T-type rectifier and the active power decoupling (auxiliary) circuit as well as the analysis of ripple energy and the dc-link capacitor. MATLAB 2019b software was used to create the system model and to conduct the following analyses.

A. MATHEMATICAL MODEL OF THE SINGLE-PHASE T-TYPE RECTIFIER

Fig. 1 shows the single-phase T-type rectifier with the 2ω ripple reduction auxiliary circuit. In this topology, the output voltage (V_{dc}) must be higher than the peak value of the input voltage source (v_s) to ensure a proper control of the input current. Therefore, the proposed system works like a boost converter.

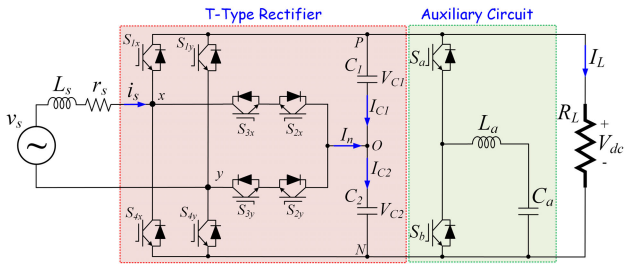

FIGURE. 1. Single-phase T-type rectifier with an active power decoupling circuit (auxiliary circuit).

It is clearly seen that the rectifier part consists of eight active power switches (four switches per-leg). The state of each switch is defined as

$$S_{ij} = \begin{cases} 1 & ON \\ 0 & OFF \end{cases} \tag{1}$$

where $i = 1,\ 2,\ 3,\ 4$ and $j = x,\ y$. The rectifier produces three various pole voltages ($+V_{dc}/2$, 0, and $-V_{dc}/2$) with respect to the switching states as shown in Table 1 [25]. The current that flows from the T-type rectifier to the load is defined as the positive current. According to the current direction and switching state, there are six current paths that are depicted in Fig. 2 [19]. The switching functions of the rectifier can be defined as

$$\left.\begin{aligned} S_1 &= S_{1x} - S_{1y} \\ S_2 &= S_{2x} - S_{2y} \end{aligned}\right\} \tag{2}$$

TABLE 1. Relationship Among the Pole Voltage and Switching States.

S_{1j}	S_{2j}	S_{3j}	S_{4j}	Pole Voltage	Operating State
ON	ON	OFF	OFF	$+0.5V_{dc}$	P
OFF	ON	ON	OFF	0	O
OFF	OFF	ON	ON	$-0.5V_{dc}$	N

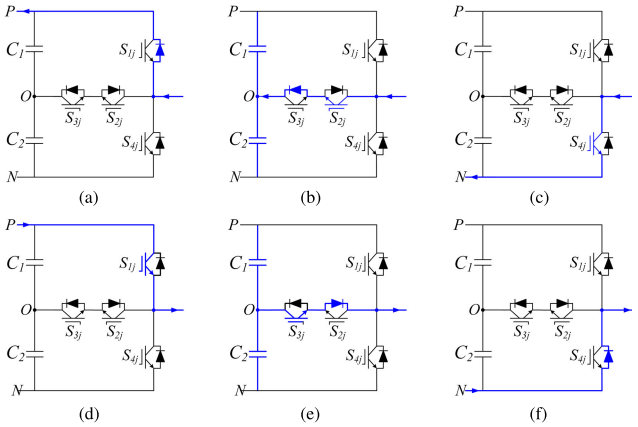

FIGURE. 2. Current paths according to the current direction and switching state when $i_s > 0$; (a) "P," (b)"O," (c)"N" and when $i_s < 0$; (d) "P," (e)"O," (f)"N".

The input voltage and neutral current can be defined in terms of the switching functions as follows

$$v_{xy} = S_1 V_{C1} + S_2 V_{C2} \tag{3}$$

$$I_n = I_{C2} - I_{C1} = (S_2 - S_1) i_s \tag{4}$$

From Fig. 1, the equations of the T-type PWM rectifier can be written as

$$v_s = L_s \frac{di_s}{dt} + r_s i_s + v_{xy} \tag{5}$$

$$I_{C1} = C_1 \frac{dV_{C1}}{dt}, \quad I_{C2} = C_2 \frac{dV_{C2}}{dt} \tag{6}$$

Since $V_{dc} = V_{C1} + V_{C2}$ and assuming that both capacitors on the dc-link have the same capacitance and are exposed to the same voltage ($V_{C1} = V_{C2} = V_{dc}/2$), the capacitor currents are equal but opposite as

$$I_{C2} = -I_{C1} \tag{7}$$

The capacitor currents in terms of the switching functions and grid current are obtained as

$$I_{C1} = \frac{1}{2}(S_1 i_s - S_2 i_s) \tag{8}$$

$$I_{C2} = \frac{1}{2}(S_2 i_s - S_1 i_s) \tag{9}$$

The derivative of grid current can be obtained from (5) as

$$\frac{di_s}{dt} = \frac{1}{L_s}(v_s - v_{xy} - r_s i_s) \tag{10}$$

where r_s is the internal resistance of the L_s.

B. RIPPLE ENERGY ANALYSIS

To investigate the double-line frequency (2ω) ripple energy on the single-phase systems, the following analyses have been conducted based on [1]. The input voltage v_s and the input current i_s are assumed to be sinusoidal and these can be represented as

$$v_s = V_s \sin \omega t \tag{11}$$

$$i_s = I_s \sin(\omega t - \theta) \tag{12}$$

where V_s is the peak voltage value, I_s is the peak current value, θ is the angle between V_s and I_s, and ω denotes the angular frequency of the input voltage supply. The input power can be formulated as

$$P_{in} = v_s(t)\, i_s(t) = \frac{V_s I_s}{2}\cos\theta - \frac{V_s I_s}{2}\cos(2\omega t - \theta) \tag{13}$$

Using basic energy and power statements, the input inductor L_s energy and power can be written as

$$\left.\begin{aligned} E_{L_s} &= \tfrac{1}{2} L_s i_s^2(t) = \tfrac{1}{2} L_s I_s^2 \sin^2(\omega t - \theta) \\ P_{L_s} &= \omega L_s I_s^2 \sin(\omega t - \theta)\cos(\omega t - \theta) \end{aligned}\right\} \tag{14}$$

The rectifier input power can be found by subtracting (13) and (14)

$$p_{in} = \underbrace{\frac{V_s I_s}{2}\cos\theta}_{P_o} - \underbrace{\left(\frac{V_s I_s}{2}\cos(2\omega t - \theta) + \frac{\omega L_s I_s^2}{2}\sin(2\omega t - 2\theta)\right)}_{P_r} \tag{15}$$

It can be seen that the rectifier input power has two components, namely a constant power P_o and a ripple power P_r. The constant power P_o supplies the dc load R_L, whereas the ripple power P_r is the 2ω ripple power, which can be expressed in the following form.

$$P_r = \sqrt{\frac{V_s^2 I_s^2}{4}\cos^2\theta + \left(\frac{\omega L_s I_s^2}{2} - \frac{V_s I_s}{2}\sin\theta\right)^2}\,\sin(2\omega t - 2\theta + \psi) \tag{16}$$

where

$$\psi = \arctan\left(\frac{\frac{V_s I_s}{2}\cos\theta}{\frac{\omega L_s I_s^2}{2} - \frac{V_s I_s}{2}\sin\theta}\right)$$

The rectifier in Fig. 1 is assumed to be lossless; then the rectifier output power P_o equals the constant power in (15). By this assumption, the peak input current is

$$I_s = \frac{2P_o}{V_s \cos\theta} \tag{17}$$

By using the 2ω ripple power in (16) and the peak input current in (17), the 2ω ripple energy can be expressed as

$$E_r = \frac{\sqrt{P_o^2 + \left(\left(2\omega L_s P_o^2 / V_s^2 \cos^2\theta\right) - P_o(\sin\theta/\cos\theta)\right)^2}}{\omega} \tag{18}$$

TABLE 2. Parameters of the single-phase T-type rectifier.

Parameter	Value
Nominal input voltage (v_s)	$120\sqrt{2}$ V
Nominal supply frequency (f_s)	50 Hz
Input inductor (L_s, r_s)	3 mH, 0.05 Ω
DC-link capacitors (C_1 and C_2)	100 μF
Auxiliary capacitor (C_a)	120 μF
Auxiliary inductor (L_a)	50 μH
DC-link voltage (V_{dc})	300 V

To eliminate this 2ω ripple energy, an alternative energy storage component such as capacitor and inductance can be used in the system. The parameters of the single-phase T-type rectifier given in Fig. 1 are summarized in Table 2. To investigate the system components on the ripple energy, the following analyses are performed [1].

The 3D graph in Fig. 3 (a) illustrates the relationship among the supply frequency, the phase angle, and the ripple energy under the constant 3-mH input inductor. It can be seen from the data in Fig. 3 (a) that the frequency has a significant impact on the ripple energy. What is interesting about the data is in this figure that the nominal frequency (50 Hz) and the unity power factor operation result in the highest 2ω ripple energy ($E_r = 38.04\ J$). This is the case the T-type rectifier operates under the system parameters in Table 2 without the auxiliary circuit.

To investigate the impact of the input inductor on the ripple energy, the power angle and the input inductance values are changed gradually under a constant supply frequency (50 Hz). The result of the analysis is set out in Fig. 3 (b). The most interesting aspect of this graph is that the 2ω ripple energy reaches its maximum value when the power factor is unity and the input inductance is 3-mH. Although reducing the input inductance causes less ripple energy, this increases the total harmonic distortion (THD) value of the input current. Looking at Figs. 3 (a) and (b), it is apparent that the minimum 2ω ripple energy value is $E_r = 38.04$ J under the system parameters given in Table 2, regardless of dc-link capacitor value and rectifier topology.

C. DC-LINK CAPACITOR ANALYSIS

Although the capacitors and the inductors are well-known energy storage components, the capacitors show better characteristics in terms of energy density for an application using a few hundred hertz [1]. For that reason, in this study, the capacitor was selected to eliminate the 2ω ripple energy that was determined in (18). Due to the nature of the capacitors, the capacitor voltage fluctuates between the minimum and maximum values in the charging and discharging cycles. Thus, the capacitor voltage fluctuation makes it capable of absorbing ripple power in (15). The dc-link voltage ripple ΔV_{dc} is

$$\Delta V_{dc} = \frac{\sqrt{P_o^2 + \left(\left(2\omega L_s P_o^2 / V_s^2 \cos^2\theta\right) - P_o(\sin\theta/\cos\theta)\right)^2}}{2V_{dc} C_{12}\omega} \tag{19}$$

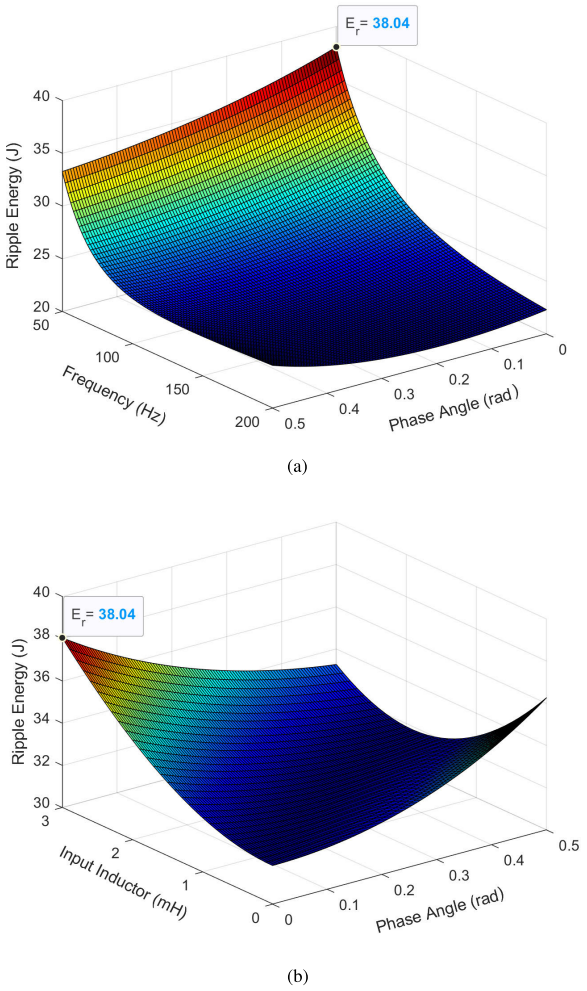

FIGURE. 3. (a) Ripple energy versus supply frequency and phase angle; (b) Ripple energy versus input inductor and phase angle.

where C_{12} is the dc-link capacitor. To assure 2% voltage ripple on the dc-link, C_{12} is calculated as 3.17 mF based on (19) and with the following specifications $V_s = 120\sqrt{2}\,V$, $P_o = 10\,kW, f_s = 50\,Hz$, $V_{dc} = 300\,V$, and $\theta = 0°$.

To investigate the impact of the auxiliary circuit in the power ripple and dc-link capacitor size, the following analysis is conducted. Now, suppose the ripple power goes to the capacitor that can be expressed as

$$P_r = \hat{P}_r sin(2\omega t) \tag{20}$$

where $\hat{P}_r$ is the peak ripple power. By using a power equilibrium relationship, the differential equation of the auxiliary capacitor voltage (V_{C_a}) can be expressed as

$$\frac{dV_{C_a}^2}{dt} = \frac{2\hat{P}_r}{C_a} sin(2\omega t) \tag{21}$$

The auxiliary capacitor voltage can be found by solving (21)

$$V_{C_a} = \sqrt{\frac{\hat{P}_r}{C_a\omega}(k - cos2\omega t)} \tag{22}$$

By using (20) and (22), then, the auxiliary capacitor current can be written as

$$i_{C_a} = \frac{\hat{P}_r sin2\omega t}{\sqrt{(\hat{P}_r/C_a\omega)(k - cos2\omega t)}} \tag{23}$$

where $k = (C_a\omega\hat{V}_{C_a}^2/\hat{P}_r) - 1,\ k \geqslant 1$. The coefficient k is defined as the energy storage margin coefficient [1]; its physical meaning can be stated by

$$\frac{k+1}{2} = \frac{\hat{E}_{C_a}}{E_r} \tag{24}$$

To better understand the impact of the energy storage margin coefficient, the voltage and current waveform for various k values are plotted in Fig. 4 based on (22) and (23). Looking at Fig. 4, it is apparent that the capacitor is entirely charged and discharged when k is 1. It means that the energy stored in the capacitor is equal to the ripple energy. On the other hand, increasing k results in more sinusoidal voltage ripple and capacitor current, which means the more excess energy that is not used is stored in the system. From this analysis, we can see that the auxiliary capacitor voltage can be charged from zero to peak value when k is 1. Based on this value, the minimum auxiliary capacitor size can be calculated by

$$C_a = \frac{2\hat{P}_r}{\hat{V}_{C_a}^2\omega} \tag{25}$$

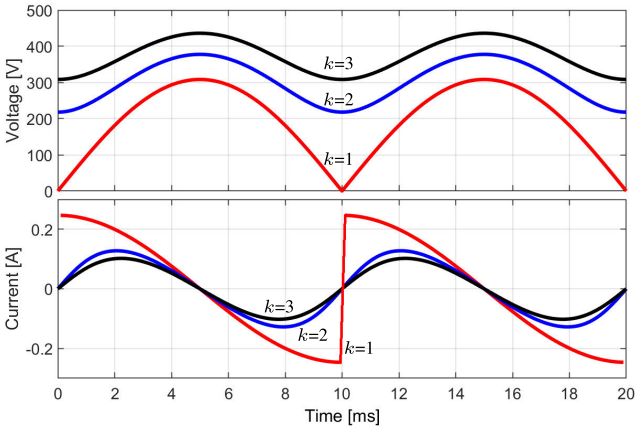

FIGURE. 4. Voltage and current waveforms of the capacitor for various k.

As mentioned before, traditionally a bulk dc-link capacitor is used to limit the ripple energy based on (19) whereas the active technique is employed to entirely charge and discharge the auxiliary capacitor to limit the ripple energy [1]. Fig. 5 displays the capacitance size comparison between C_{12} and C_a. The calculations are based on (19) for the traditional technique and on (24) for the active technique. As shown in Fig. 5, one horizontal coordinate is the dc-link voltage ripple and another horizontal coordinate is the dc-link voltage value that the auxiliary capacitor is entirely charged and discharged. The most striking result to emerge from the data is that the capacitance in the active technique is 37.5 times smaller

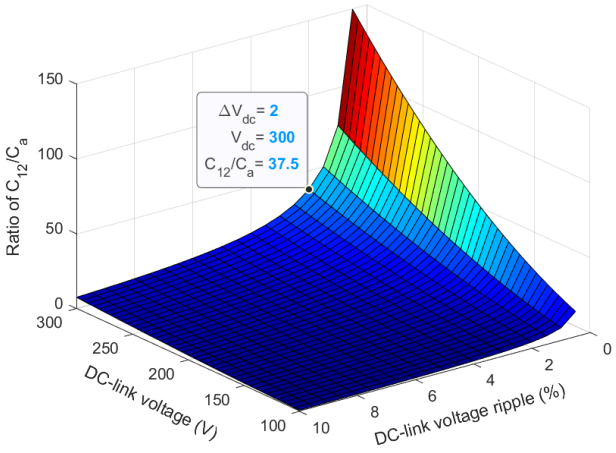

FIGURE. 5. Capacitance comparison results between the traditional and active techniques.

than the traditional technique with 2% dc-link voltage ripple requirement. Please remember that the C_{12} was calculated as 3.17 mF based on (19) to assure 2% voltage ripple on the dc-link. By using active method, the capacitor size can be reduced from 3.17 mF to 84.5 μF. To leave some margin, 120 μF auxiliary capacitor C_a is used in the system. Please note that the dc-link capacitors (C_1 and C_2) are still required for filtering the high-frequency ripple. However, their size is significantly smaller than in the traditional technique. For that reason, in this study, the dc-link capacitors (C_1 and C_2) are selected as 100 μF.

D. AUXILIARY CIRCUIT OPERATION

The auxiliary (power decoupling) circuit is connected at the dc-link of the single-phase T-type rectifier, as depicted in Fig. 1. The auxiliary circuit is composed of two power switches, the auxiliary capacitor C_a, and the auxiliary inductor L_a that transfers the ripple energy between the C_a and the dc-link. It is worth mentioning that the main converter (T-type rectifier) regulates the dc-link voltage, whereas the auxiliary circuit controls the ripple power in (16).

The operation mode of the auxiliary circuit depends on the energy transfer between the dc-link and the C_a. The operation modes and waveforms of the auxiliary circuit are given in Figs. 6 (a) and (b), respectively. In buck mode, the switch S_a is controlled to transfer the ripple energy from the dc-link to the C_a. The dc-link charges both the L_a and C_a during the turn-on interval of S_a, whereas the L_a release its energy to the C_a during the turn-off interval of S_a. In boost mode, the switch S_b is controlled to release the energy from the C_a to the dc-link. The L_a is charged by the C_a during the turn-on interval of S_b, whereas the both the C_a and L_a release energy back to the dc-link during the turn-off interval of S_b.

III. PROPOSED MODEL PREDICTIVE CONTROL

Fig. 7 depicts the block diagram of the proposed control technique. The lack of a grid voltage sensor and the fulfillment of many objectives reveals the value of the presented

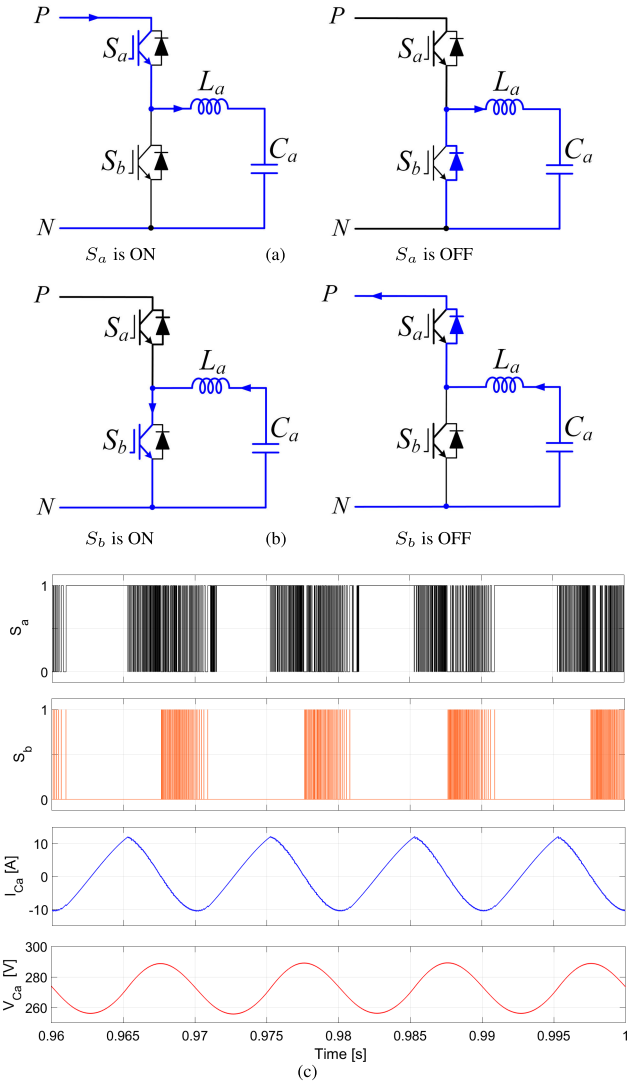

FIGURE. 6. The operation modes and waveforms of the auxiliary circuit. (a) buck-mode, (b) boost-mode, (c) waveforms.

method. The proposed control technique consists of four main parts, including sensorless grid voltage estimation, reference current generation based on power equilibrium, MPC for the main converter, and MPC for the power decoupling circuit based on instantaneous ripple power control.

A. SENSORLESS GRID VOLTAGE ESTIMATION

The grid voltage estimation is based on MRAS that is a very attractive solution for sensorless motor drives. The main idea behind MRAS is to design a closed-loop controller with parameters that can be updated to change the response of the system [26]. In MRAS, two independent models, namely, reference and adaptive models, are used to compute the same variable. First, the output of the adaptive model is compared to the response of the reference model. Then, the suitable controller is used to minimize the error between the adaptive model output and the reference model output. Finally,

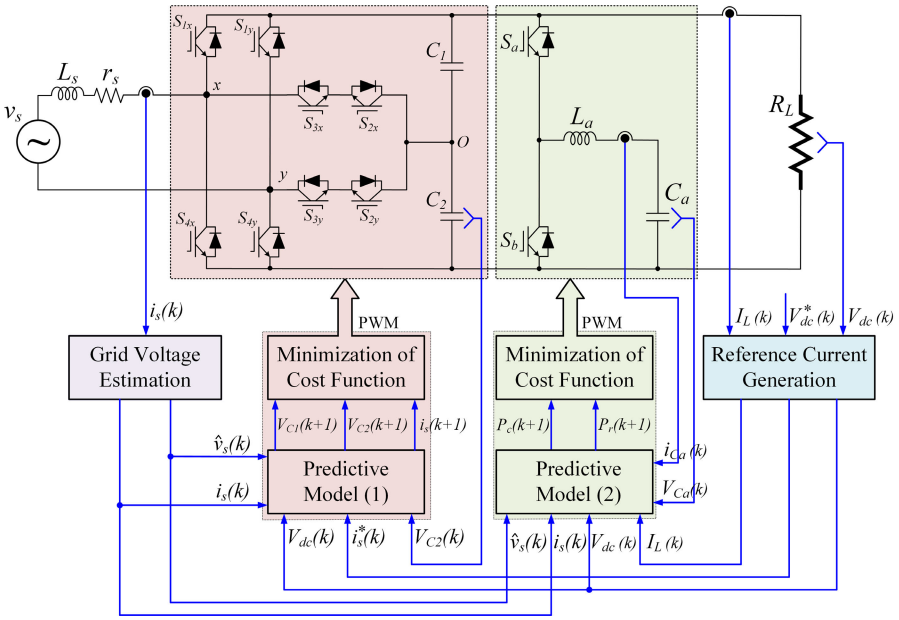

FIGURE. 7. Control diagram of the proposed grid-voltage sensorless MPC technique.

the controller output drives the parameter in the adaptive model that leads to the adaptive model response to match the response of the reference model.

The proposed estimation technique uses active and reactive power exchange between the grid and the rectifier. The reference model for active P_1 and reactive Q_1 powers can be obtained by using a fictitious two-phase ($\alpha - \beta$) reference frame.

$$\left.\begin{aligned} P_1 &= \tfrac{1}{2}\left(v_{xy\alpha} i_{s\alpha} + v_{xy\beta} i_{s\beta}\right) \\ Q_1 &= \tfrac{1}{2}\left(v_{xy\beta} i_{s\alpha} - v_{xy\alpha} i_{s\beta}\right) \end{aligned}\right\} \tag{26}$$

where v_{xy} is the rectifier input voltage and it is defined in (3) and i_s is the grid current.

The T-type rectifier is connected to the grid through the input inductance L_s, as shown in Fig. 7. In such a system, by neglecting the internal resistance r_s the active P_2 and reactive Q_2 powers can be derived as

$$\left.\begin{aligned} P_2 &= \frac{V_{xy} V_s \sin\delta}{2X_{Ls}} \\ Q_2 &= \frac{V_{xy}^2 - V_{xy} V_s \cos\delta}{2X_{Ls}} \end{aligned}\right\} \tag{27}$$

It can be seen that the reference model for active and reactive powers can be computed by (26) where all the variables can be measured or calculated. It is also clear that (26) is independent of the grid voltage. On the other hand, although, (27) can be used to calculate the same active and reactive powers, it depends on the grid voltage amplitude V_s and phase angle δ. For that reason, (27) can be used as the adaptive model. The computed results of (26) and (27) should be identical under steady-state conditions. By using this knowledge, the grid voltage can be estimated.

The block diagram of the MRAS based grid voltage observer is given in Fig. 8. The error between the reference

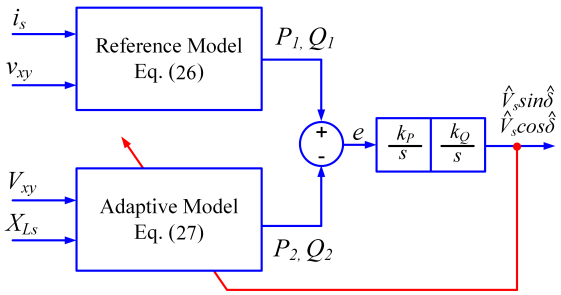

FIGURE. 8. Block diagram of MRAS based grid voltage observer.

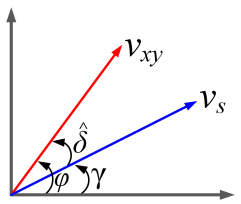

FIGURE. 9. Phasor representation of the grid voltage (v_s) and the rectifier input voltage (v_{xy}).

model (26) and the adaptive model (27) is processed using a suitable controller to get an accurate estimation of the grid voltage. The estimated $\hat{V}_s sin\hat{\delta}$ and $\hat{V}_s cos\hat{\delta}$ can now be used to compute the unit vectors $cos\gamma$ and $sin\gamma$. $\hat{\delta}$ is the angle between the v_s and v_{xy} and the angle γ is equal to $\varphi - \hat{\delta}$ as shown in Fig. 9. Trigonometric identities can be used to calculate the unit vectors as

$$\left.\begin{aligned} \cos\gamma &= \cos\varphi\cos\hat{\delta} + \sin\varphi\sin\hat{\delta} \\ \sin\gamma &= \sin\varphi\cos\hat{\delta} - \cos\varphi\sin\hat{\delta} \end{aligned}\right\} \tag{28}$$

where

$$\cos\varphi = \frac{v_{xy\alpha}}{V_{xy}}, \quad \sin\varphi = \frac{v_{xy\beta}}{V_{xy}},$$
$$\cos\hat{\delta} = \frac{\left(\hat{V}_s\cos\hat{\delta}\right)}{\hat{V}_s}, \quad \sin\hat{\delta} = \frac{\left(\hat{V}_s\sin\hat{\delta}\right)}{\hat{V}_s},$$

where

$$V_{xy} = \sqrt{\left(v_{xy\alpha}\right)^2 + \left(v_{xy\beta}\right)^2},$$
$$\hat{V}_s = \sqrt{\left(\hat{V}_s\cos\hat{\delta}\right)^2 + \left(\hat{V}_s\sin\hat{\delta}\right)^2}.$$

Unit vectors $cos\gamma$ and $sin\gamma$ in (28) are the same as the unit vectors generated from a traditional phase-locked-loop (PLL) structure. Finally, the estimated grid voltage can be expressed as

$$\hat{v}_s = \hat{V}_s\cos\gamma. \tag{29}$$

B. REFERENCE CURRENT GENERATION

In this study, the reference current generation is based on the energy equilibrium between ac-side and dc-side instead of the PI controller. Due to the reduced blocking voltage, the middle switch in the T-type topology shows very low switching losses, and the input impedance is low. Therefore, the inductor core loss and switching loss can be very small. By neglecting power losses in the rectifier, the power equations of the ac-side and dc-side can be expressed as

$$\underbrace{\frac{V_s I_s^*}{2} - r_s\left(\frac{I_s^*}{\sqrt{2}}\right)^2}_{P_{ac}} = \underbrace{\frac{V_{dc}^2}{R_L}}_{P_{dc}} \tag{30}$$

The reference line current (I_s^*) can be derived from (30) as

$$I_s^* = \frac{V_s}{2r_s} - \sqrt{\left(\frac{V_s}{2r_s}\right)^2 - \frac{2V_{dc}^2}{r_s R_L}} \tag{31}$$

In (31), the grid voltage V_s is estimated from (29), the dc-link voltage V_{dc} is measured by the voltage sensor, and the internal resistance r_s value can be identified by LC meter. On the other hand, the output resistance R_L is unknown in this equation since this value depends on the output load. To estimate the output resistance R_L, Ohm's law in (32) is employed due to its simplicity.

$$\hat{R}_L = \frac{V_{dc}}{I_L} \tag{32}$$

However, the estimation in (32) goes to infinity when I_L is zero at the start-up. For that reason, supposing that at steady-state operating conditions, the rectifier maintains the target dc-link voltage with unity power factor, it is crucial to determine the initial value for R_L.

C. MPC FOR THE T-TYPE RECTIFIER

It is well known that the main aim of the PWM rectifier controller is to regulate the amplitude of the output voltage and ensure the unity power factor by forcing semiconductor switches to follow the grid voltage using the PLL loop. Apart from these control requirements, the T-type rectifier requires to maintain the dc-link capacitors voltages balance ($V_{C1} \approx V_{C2} \approx V_{dc}/2$) that play a critical role in the success of the overall control. Therefore, the MPC is used for control of T-type rectifier since it is a multivariable control algorithm and tackles multiple control objectives in a single cost function.

The line current tracking and dc-link voltage regulation are two control objectives for the presented MPC technique. These control objectives can be formulated through the cost function to minimize the error between the control variables and their references. Considering that the two controlled variables (line current and dc-link voltage) are tightly coupled. The cost function of the T-type rectifier consists of the following components:

$$g_1 = \left|i_s^*(k+1) - i_s(k+1)\right|^2 + \lambda\left|V_{C1}(k+1) - V_{C2}(k+1)\right| \tag{33}$$

where $i_s^*(k+1)$, $i_s(k+1)$, and $V_{C1}(k+1)$ and $V_{C2}(k+1)$ indicate the reference line current, the predicted line current, and the predicted dc-link capacitor voltages at an instant $(k+1)$, respectively. In (33), the first term is the current tracking error and the second term is the voltage deviation of the dc-link capacitors. The weighting factor λ is used to handle the relationship between reference current tracking and midpoint voltage balance.

Because of its simplicity, the future behavior of the control variables is obtained by the forward Euler technique as

$$\frac{dx}{dt} \approx \frac{x(k+1) - x(k)}{T_s} \tag{34}$$

where T_s is sampling time.

By approximating (10) with (34), the discrete-time model of the line current can be obtained as

$$i_s(k+1) = i_s(k) + \frac{Ts}{L}\left(\hat{v}_s(k) - v_{xy}(k) - r_s i_s(k)\right) \tag{35}$$

Similarly, the discrete-time model of the dc-link capacitors voltages can be expressed as

$$\left.\begin{aligned} V_{C1}(k+1) &= V_{C1}(k) + \tfrac{T_s}{2C_1}\left[S_1(k)i_s(k) - S_2(k)i_s(k)\right] \\ V_{C2}(k+1) &= V_{C2}(k) + \tfrac{T_s}{2C_2}\left[S_2(k)i_s(k) - S_1(k)i_s(k)\right] \end{aligned}\right\} \tag{36}$$

The algorithm of the MPC for the main converter is given in Algorithm 1. The first step is to set required initial parameters such as L_s, r_s, C_1, C_2, and then the switching states and pole voltages were defined for using into the predictive block (for-loop). The second step is to predict the future line current $i_s(k+1)$ and dc-link capacitor voltages $V_{C1}(k+1)$ and $V_{C2}(k+1)$ using the measured values of i_s, V_{C_2}, V_{dc}, and I_L at the instant k and the estimated grid voltage $\hat{v}_s$. After that,

Algorithm 1 MPC for the Main Converter

Input: i_s^*, i_s, $\hat{v}_s$, V_{C_2}, V_{dc}, I_L
Output: S_{1x}, S_{2x}, S_{1y}, S_{2y}
set initial values;
states = [1111; 0111; 0011;.....; 1100; 0100; 0000];
v = [0;$-0.5V_{dc}$;-V_{dc};$0.5V_{dc}$;0;$-0.5V_{dc}$;V_{dc};$0.5V_{dc}$;0];
$V_{C1} = V_{dc} - V_{C2}$;
for j = *length(v)* **do**
  $i_s(k+1) = i_s(k) + ((T_s/L_s) * (\hat{v}_s - v(j) - (r_s * i_s)))$;
  $V_{C1}(k+1) = V_{C1}(k) + ((states(i,2) - states(i,1) - states(i,4) + states(i,3))(T_s(-i_s - I_L))/(2C_1))$;
  $V_{C2}(k+1) = V_{C1}(k) + ((states(i,2) - states(i,1) - states(i,4) + states(i,3))(T_s(-i_s - I_L))/(2C_2))$;
  $g_2 = abs(i_s^*(k+1) - i_s(k+1))^2 + \lambda * abs(V_{C1}(k+1) - V_{C2}(k+1))$;
  if $g_1 \leq g_{opt}$ **then**
    $g_{opt} = g_1$;
    $x_{opt} = j$;
  end if
end for
S_{1x} = states(x_{opt}, 1);
S_{2x} = states(x_{opt}, 2);
S_{1y} = states(x_{opt}, 3);
S_{2y} = states(x_{opt}, 4);

the final step is to determine the switching states in Table 1 that can minimize the cost function (g_1).

D. MPC FOR THE POWER DECOUPLING CIRCUIT

The control scheme of the MPC for the power decoupling circuit is shown in Fig. 7. It is worth mentioning that the control of the power decoupling circuit is independent of the control of T-type rectifier. On the other hand, both control algorithms run as parallel in order to ensure the control objectives for the main converter and the power decoupling circuit.

The voltage on the switch S_b can take three different values $+0.5V_{dc}$, 0, and $-0.5V_{dc}$ depending on the switching state. Furthermore, by neglecting internal resistance of L_a, the voltage on the switch S_b can be expressed as

$$v_{S_b} = L_a \frac{di_{C_a}}{dt} + v_{C_a} \tag{37}$$

By substituting (34) into (37), the auxiliary capacitor current (i_{C_a}) can be predicted by

$$i_{C_a}(k+1) = i_{C_a}(k) + \frac{T_s}{L_a}\left[v_{S_b}(k) - v_{C_a}(k)\right] \tag{38}$$

The auxiliary capacitor power at the $(k+1)$ instant can be expressed by

$$\begin{aligned} P_{C_a}(k+1) &= v_{C_a}(k+1)\, i_{C_a}(k+1) \\ &= v_{C_a}(k+1)\left[i_{C_a}(k) + \frac{T_s}{L_a}\left[v_{S_b}(k) - v_{C_a}(k)\right]\right] \end{aligned} \tag{39}$$

Since the sampling time T_s is very small and it is smaller than the time constant of LC branch, we can assume that the capacitor voltage at $(k+1)$ instant is almost equal to the capacitor voltage at k instant $v_{C_a}(k+1) = v_{C_a}(k)$. Therefore, the discrete-time model of the auxiliary capacitor power can be written as

$$P_{C_a}(k+1) = v_{C_a}(k)\left[i_{C_a}(k) + \frac{T_s}{L_a}\left[v_{S_b}(k) - v_{C_a}(k)\right]\right] \tag{40}$$

The instantaneous power from the ac source was given in (13) and assuming the active power is P_{dc}, then, the instantaneous ripple power is

$$P_r = v_s(k)\, i_s(k) - P_{dc} \tag{41}$$

Finally, the cost function for the power decoupling circuit is defined as

$$g_2(k) = \left|P_r(k+1) - P_{C_a}(k+1)\right| \tag{42}$$

The developed MPC algorithm for the power decoupling circuit is given in Algorithm 2. The first step is to set required initial parameters such as L_a and C_a, and then the switching states and the voltage vector were defined for using into the predictive block (for loop). The second step is to predict the future ripple power $P_r(k+1)$ and the auxiliary capacitor power $P_{Ca}(k+1)$ using the measured values of i_s, i_{ca}, v_{ca}, V_{dc}, and I_L at the instant k and the estimated grid voltage $\hat{v}_s$. After that, as it was mentioned before, the final step is to determine the switching combination that can minimize the cost function g_2.

Algorithm 2 MPC for the Power Decoupling Circuit

Input: i_s, $\hat{v}_s$, i_{C_a}, v_{C_a}, I_L, V_{dc}
Output: S_a, S_b
set initial values;
states = [01; 10; 00; 11];
$v_{S_b} = [-0.5V_{dc};\ 0.5V_{dc};\ 0;\ 0]$;
$P_{dc} = V_{dc}I_{dc}$;
for *j=length(v)* **do**
  $P_r(k+1) = (i_s * \hat{v}_s) - P_{dc}$;
  $P_c(k+1) = v_{C_a}{}^*[i_{C_a} + (T_s/L_a)^*(v_{S_b}(j) - v_{C_a})]$;
  $g_2 = abs(P_r(k+1) - P_c(k+1))$;
  if $g_2 \leq g_{opt}$ **then**
    $g_{opt} = g_2$;
    $x_{opt} = j$;
  end if
end for
S_a = states(x_{opt}, 1);
S_b = states(x_{opt}, 2);

IV. EXPERIMENTAL VERIFICATION

To verify the effectiveness of the proposed control technique, a prototype of the single-phase T-type rectifier with the active power decoupling circuit is implemented as depicted

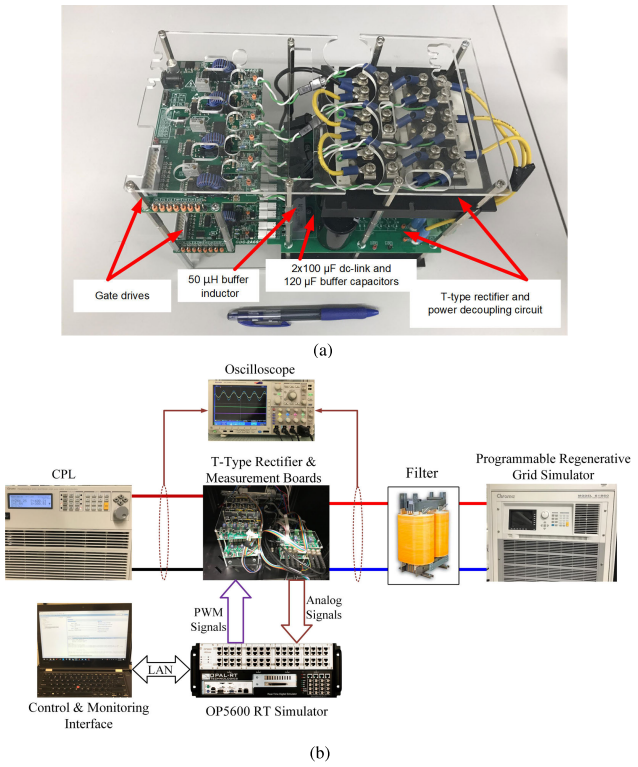

FIGURE. 10. Experimental setup; (a) T-type rectifier prototype picture; (b) test-bench structure.

in Fig. 10 (a). Furthermore, the test-bench structure for the experiments is illustrated in Fig. 10 (b). For ac-side, a variable-frequency power source has been used to emulate the single-phase voltage and an inductor is utilized as the input filter inductance. A programmable electronic load, which has constant resistance load (CRL) and constant power load (CPL) capabilities, has been used as the dc load. Furthermore, three voltage sensors LV25-P combined with three current sensors LA100-P are utilized to measure the required voltages and currents, respectively. The developed controller is implemented on the OPAL-RT OP-5600 platform with the sampling time $T_s = 20\ \mu s$.

A. STEADY-STATE ANALYSIS

Figs. 11-14 illustrate the steady-state results of the proposed system. To highlight the reduction of 2ω ripple power, the proposed solution was compared with the single-phase T-type rectifier without decoupling functionality. For all cases, the reference dc-link voltage is set at 300 V and the output load is set at 30 Ω.

Fig. 11 (a) shows the steady-state performance of the system when the decoupling function is enabled. It is clearly seen that the grid voltage (v_s) and the grid current (i_s) are in the same phase. In other words, the single-phase T-type rectifier operates with unity power factor. It is also shown that the V_{dc} tracks its reference (V_{dc}^*) with high accuracy and nearly zero steady-state error. Furthermore, the capacitor voltages (V_{C1} and V_{C2}) are balanced at 150V that is half of the dc-link voltage. In this operation, the decoupling circuit

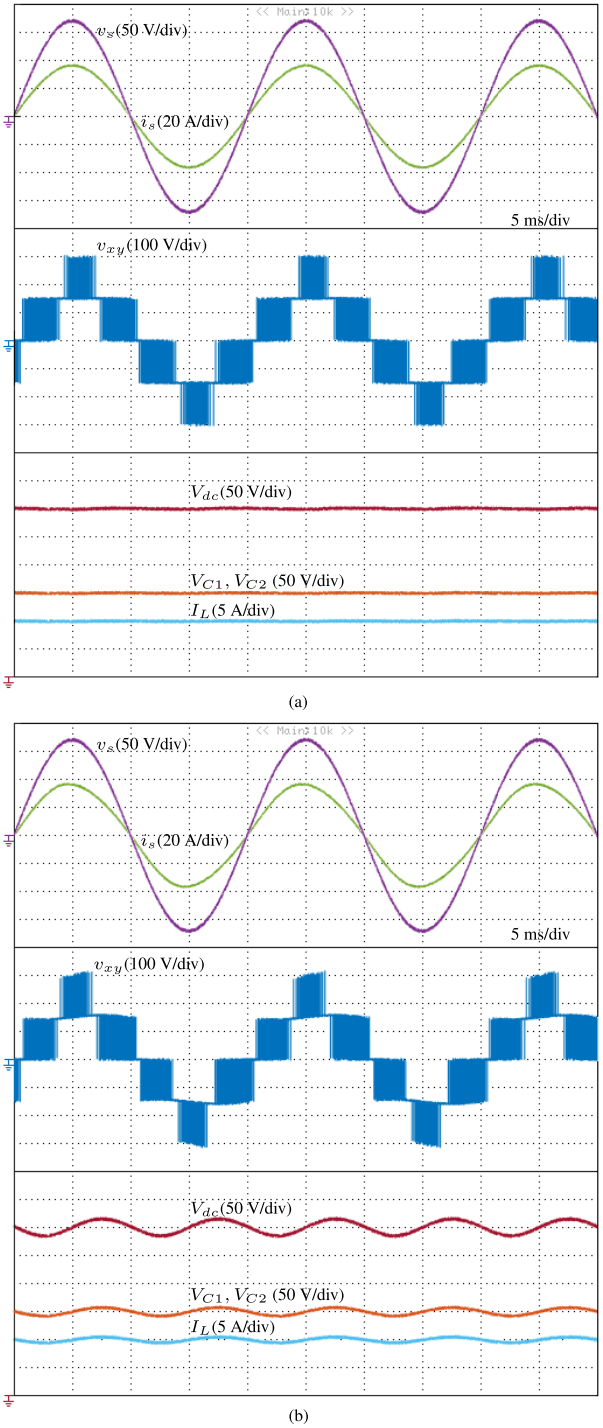

FIGURE. 11. Experimental results of the steady-state analysis (a) with decoupling function; (b) without decoupling function.

is active, and almost all the ripple energy is stored in the auxiliary capacitor (C_a) as shown in Fig. 12. Fig. 11 (b) shows the steady-state performance when the decoupling function is disabled. Although, the unity power factor objective is satisfied in this operation mode, a large dc-link voltage ripple (approximately 50 V) was observed since all of the 2ω ripple energy goes to the small dc-link capacitor.

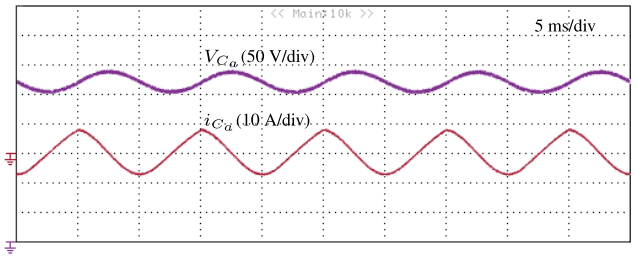

FIGURE. 12. Experimental results of the steady-state analysis of auxiliary circuit voltage (V_{Ca}) and current (i_{Ca}) when the decoupling function is active.

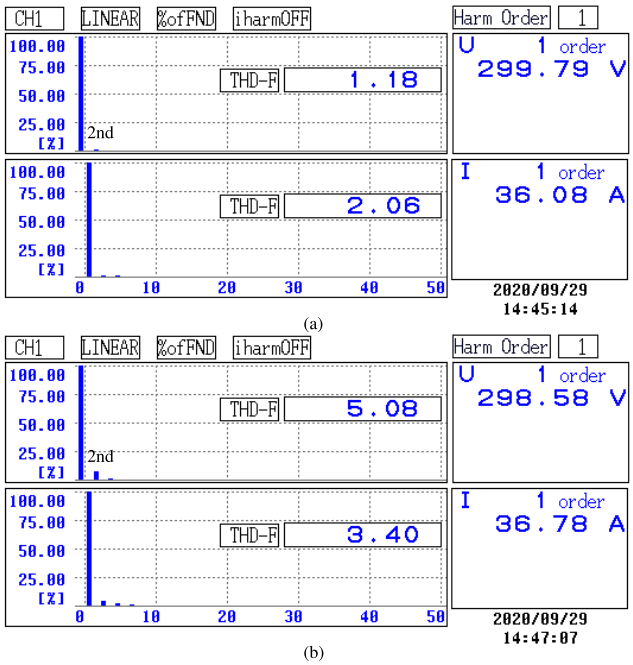

FIGURE. 13. Experimental results of FFT analysis (a) with decoupling function; (b) without decoupling function.

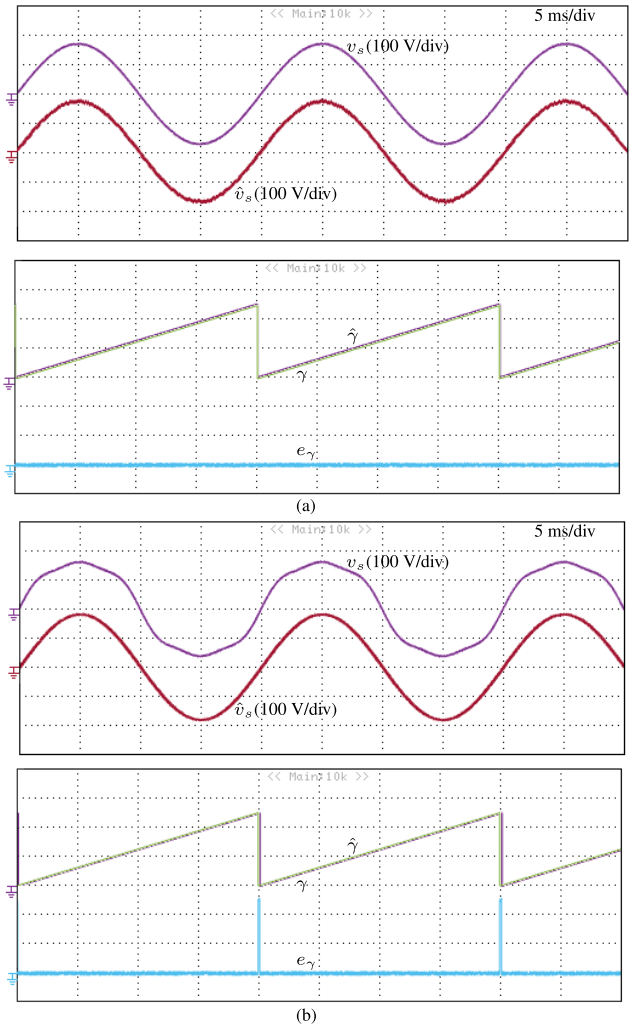

FIGURE. 14. Experimental results of the actual grid voltage (v_s), the actual grid voltage angle (γ), the estimated grid voltage ($\hat{v}_s$), the estimated grid voltage angle ($\hat{\gamma}$), and the error between the actual and estimated voltage angles (e_γ); (a) under normal grid conditions; (b) under distorted grid conditions.

Fig. 13 (a) and (b) show the harmonic analysis of the output voltage (V_{dc}) and the input current (i_s) with and without decoupling function. It is observed that the current harmonic levels in both cases are significantly lower than the limits mentioned by international power quality standards like IEEE Std 519. However, there is 2ω frequency components on the dc-link voltage when the decoupling function is not active as shown in Fig. 13 (b).

To prove the superiority of the proposed grid voltage sensorless control algorithm, the tests were conducted under normal and distorted grid voltage conditions. The estimated grid voltage ($\hat{v}_s$) for a purely sinusoidal grid voltage (v_s) signal is shown in Fig. 14 (a). The grid voltage signal (v_s) is then mixed with harmonic components and the estimation under distorted grid voltage is reported in Fig. 14 (b). It can be seen that the proposed voltage sensorless estimation technique is able to extract the fundamental voltage signal in both cases. Furthermore, the estimated voltage angle tracks the actual voltage angle with high accuracy for both cases. It is clear that the error in estimating grid voltage angle results in both cases is almost zero, showing an excellent position tracking performance.

B. ROBUSTNESS ANALYSIS

To verify the robustness of the proposed control strategy, several tests have been conducted under various working conditions. The results are given in Figs. 15–17.

1) LOAD VARIATION

In this test, the programmable load is operated in CRL mode and the output resistance (R_L) is reduced from 30 Ω to 15 Ω. During this test, the reference dc-link voltage is set at 300 V. Fig. 15 (a) shows the dynamic response of the system when the decoupling function is active. The output voltage is regulated at 300V and is almost not affected by this sudden

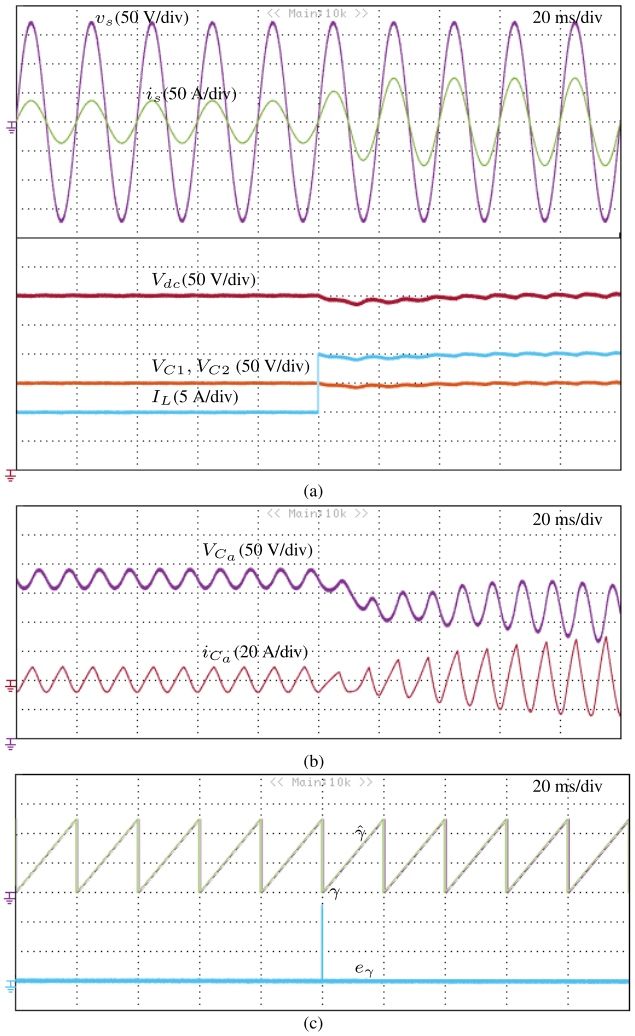

FIGURE. 15. Experimental results of the dynamic response (a) main circuit; (b) auxiliary circuit when the decoupling function is enabled; (c) voltage estimation.

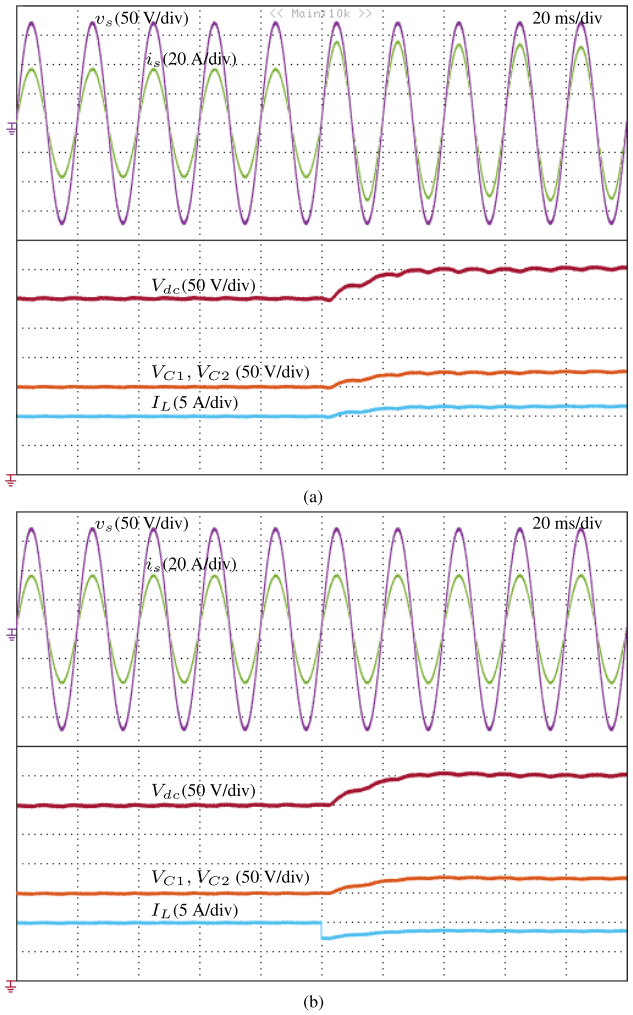

FIGURE. 16. Experimental results of the dynamic response (a) with CRL; (b) with CPL.

100% load increase. Although the amplitude of the 2ω ripple increased, the dc-link voltage ripple is within the required 2% limit. Thus, R_L variation seems not to affect the proposed technique. The performance of the decoupling circuit is shown in Fig. 15 (b) under the same operating conditions. The system has excellent ripple power tracking performance in both conditions and the ripple power is almost fully buffered in the decoupling circuit with the proposed control method even during the step change of load power. Furthermore, it can be seen from Fig. 15 (c) that grid voltage angle was estimated accurately by the proposed technique, even though under load step.

2) DC-LINK VOLTAGE VARIATION

In this experiment, the programmable load is operated in CRL and CPL modes. For the CRL mode, the output resistance (R_L) is set at 30 Ω. For the CPL mode, the output power (P_L) is set at 3kW. A step change of 50 V in $\hat{V}_{dc}$ is applied ($\hat{V}_{dc}$ passes from 300 to 350 V).

Fig. 16 (a) shows the dynamic performance of the system under CRL mode. It is clear that V_{dc} is regulated at 350 V while V_{C1} and V_{C2} are balanced at 175V. Furthermore, the grid voltage (v_s) and the grid current (i_s) are in the same phase for both conditions. Please note that the output power increased from 3kW to approximately 4kW since the load is in CRL mode.

Fig. 16 (b) shows the dynamic performance of the system under CPL mode. It is obvious that similar to previous case V_{dc} tracks its reference (V_{dc}^*) with high accuracy and nearly zero steady-state error and the single-phase rectifier operates with unity power factor. It is clearly seen that the output current (I_L) reduces from 10A to 8.33 A while the dc-link voltage V_{dc} increases from 300V to 350V. In this case the output power is maintained at 3kW since the load in CPL mode.

3) PARAMETERS MISMATCH

Since the controllers based on MPC, the performance of the controller may depend on the system parameters. To investigate the robustness of the proposed controller against the grid

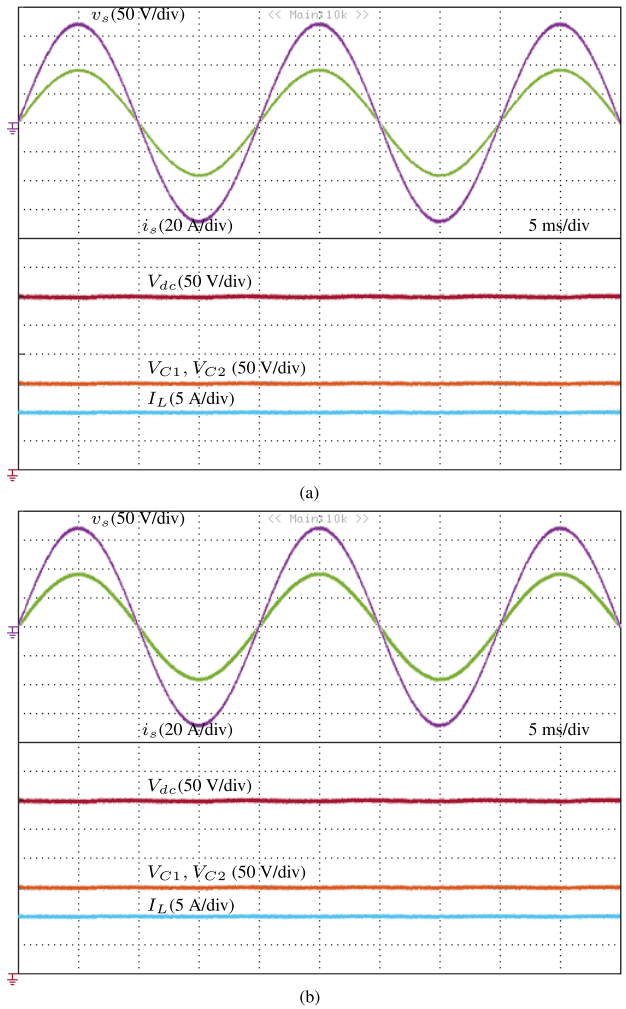

FIGURE. 17. Experimental results of the parameter variations (a) +15% variations in L_s, C_1 and C_2; (b) −15% variations in L_s, C_1 and C_2.

inductance and dc-link capacitors variations, the following cases have been considered.

Fig. 17 (a) and (b) show the experimental results of the system under ± 15% variations in L_s and the dc-link capacitors C_1 and C_2. Despite the large variations in L_s, C_1, and C_2, the controller performance is still satisfactory. In conclusion, even with the mismatch in inductance and capacitor parameters, the proposed controller handles this issue without a significant impact on the system performance and shows that relatively low sensitivity to parameter changes.

4) COST AND VOLUME ANALYSIS

To observe the effect of the 2ω ripple on the rectifier parameters, cost and volume analysis were done. For comparison purposes, the dimension and price information of some components in the designed system and in the traditional system are given in Table 3. It can be seen that the designed system requires the capacitor (C_a), inductor (L_a), and switches (S_a and S_b) for the auxiliary circuit. This circuit brings extra cost, which is around $96.5, to the system. On the other hand, using this circuit in the system reduces the dc-link capacitor size significantly, which results in cost and volume reduction in the overall system. Furthermore, the proposed control uses MRAS to estimate the grid voltage without a sensor. This also decreases the cost of the control system around $68. In addition, the volume of the capacitors in the traditional system is around 665 cm^3 whereas the total volume of the auxiliary circuit components given in the table is around 100 cm^3. It is clearly seen that using the auxiliary circuit reduces the hardware size significantly.

TABLE 3. Comparison of the designed and traditional system components.

Components		Designed system	Traditional system
C1 and C2	Specs	100 µF/450 V	3.2 mF/450 V
	Mfr. Part#	36DY101F450AN2A	550322T450DF2B
	Price	$32.11*2	$109.27*2
	Dimensions.	L: 35 mm D: 35 mm	L: 143.64 mm D: 76.81 mm
Ca	Specs	120 µF/400 V	
	Mfr. Part#	E36D401LPN121TA41M	
	Price	$8.34	
	Dimensions	L: 41 mm D: 35 mm	
La	Specs	50 µH/14A	
	Mfr. Part#	1539M13	
	Price	$13.60	
	Dimensions	L= 28.19 mm D= 30.98 mm	
Sa and Sb	Specs	High Speed IGBT	
	Mfr. Part#	IKW15N120H3FKSA1	
	Price	$5.17*2	
	Dimensions	L= 20.80 mm W= 15.70 mm H= 4.83 mm	
Voltage sensor	Specs		LEM-LV25P
	Mfr. Part#		LV 25-P
	Price		$68
	Dimensions		L= 29.2 mm W= 26 mm H= 15.2 mm

Note: Data are from Mouser and Digi-Key websites.

V. CONCLUSION

In this study, the grid voltage sensorless model predictive control technique was proposed to control the single-phase T-type rectifier while the instantaneous ripple power predictive control technique was used to minimize the 2ω ripple power of the single-phase T-type rectifier. The grid voltage was estimated through MRAS. Thus, the cost of the system was reduced by the elimination of the voltage sensor in the control loop. Furthermore, using the power decoupling circuit and its control technique in the system decreased the dc-link capacitor size that resulted in cost and volume reduction in the overall system. Experimental results on the test bench verified the proposed control technique with the following advantages:

1) fast response to the load change;
2) perfect buffering 2ω ripple power even though the rectifier input voltage distorted;
3) minimization of the dc-link capacitor requirement;
4) unity power factor all operating conditions;
5) excellent performance under CRL and CPL conditions.

Apart from these advantages the developed control structure is simple and it is cost-effective due to the absence of

a grid voltage sensor and significantly lower dc-link capacitance requirement.

ACKNOWLEDGMENT

The statements made herein are solely the responsibility of the authors.

REFERENCES

[1] R. Wang, F. Wang, D. Boroyevich, R. Burgos, R. Lai, P. Ning, and K. Rajashekara, "A high power density single-phase PWM rectifier with active ripple energy storage," *IEEE Trans. Power Electron.*, vol. 26, no. 5, pp. 1430–1443, May 2011.

[2] S. Bayhan, M. Trabelsi, and H. Abu-Rub, "Model predictive control based current ripple damping in single-phase quasi-impedance-source inverter," in *Proc. 19th Eur. Conf. Power Electron. Appl. (EPE ECCE Eur.)*, Sep. 2017, pp. 1–8.

[3] Y. Sun, Y. Liu, M. Su, W. Xiong, and J. Yang, "Review of active power decoupling topologies in single-phase systems," *IEEE Trans. Power Electron.*, vol. 31, no. 7, pp. 4778–4794, Jul. 2016.

[4] X. Cao, Q.-C. Zhong, and W.-L. Ming, "Ripple eliminator to smooth DC-bus voltage and reduce the total capacitance required," *IEEE Trans. Ind. Electron.*, vol. 62, no. 4, pp. 2224–2235, Apr. 2015.

[5] W. Liang, Y. Liu, B. Ge, H. Abu-Rub, R. S. Balog, and Y. Xue, "Double-line-frequency ripple model, analysis, and impedance design for energy-stored single-phase quasi-Z-Source photovoltaic system," *IEEE Trans. Ind. Electron.*, vol. 65, no. 4, pp. 3198–3209, Apr. 2018.

[6] Y. Tang and F. Blaabjerg, "Power decoupling techniques for single-phase power electronics systems—An overview," in *Proc. IEEE Energy Convers. Congr. Expo. (ECCE)*, Sep. 2015, pp. 2541–2548.

[7] B. Ge, X. Li, H. Zhang, Y. Liu, R. S. Balog, H. Abu-Rub, and L. Alpuerto, "Direct instantaneous ripple power predictive control for active ripple decoupling of single-phase inverter," *IEEE Trans. Ind. Electron.*, vol. 65, no. 4, pp. 3165–3175, Apr. 2018.

[8] M. Su, P. Pan, X. Long, Y. Sun, and J. Yang, "An active power-decoupling method for single-phase AC–DC converters," *IEEE Trans. Ind. Informat.*, vol. 10, no. 1, pp. 461–468, Feb. 2014.

[9] B. Ge, Y. Liu, H. Abu-Rub, R. S. Balog, F. Z. Peng, S. McConnell, and X. Li, "Current ripple damping control to minimize impedance network for single-phase quasi-Z source inverter system," *IEEE Trans. Ind. Informat.*, vol. 12, no. 3, pp. 1043–1054, Jun. 2016.

[10] M. Aly, E. M. Ahmed, and M. Shoyama, "Modulation method for improving reliability of multilevel T-type inverter in PV systems," *IEEE J. Emerg. Sel. Topics Power Electron.*, vol. 8, no. 2, pp. 1298–1309, Jun. 2020.

[11] H. Komurcugil and S. Bayhan, "Passivity-based control strategy for single-phase three-level T-type PWM rectifiers," in *Proc. IEEE 29th Int. Symp. Ind. Electron. (ISIE)*, Jun. 2020, pp. 1179–1184.

[12] S. A. Khan, Y. Guo, Y. P. Siwakoti, D. D.-C. Lu, and J. Zhu, "A disturbance rejection-based control strategy for five-level T-type hybrid power converters with ripple voltage estimation capability," *IEEE Trans. Ind. Electron.*, vol. 67, no. 9, pp. 7364–7374, Sep. 2020.

[13] S. Bayhan and H. Komurcugil, "Sliding-mode control strategy for three-phase three-level T-type rectifiers with DC capacitor voltage balancing," *IEEE Access*, vol. 8, pp. 64555–64564, 2020.

[14] T. Noguchi, H. Tomiki, S. Kondo, and I. Takahashi, "Direct power control of PWM converter without power-source voltage sensors," *IEEE Trans. Ind. Appl.*, vol. 34, no. 3, pp. 473–479, May/Jun. 1998.

[15] H. Yang, Y. Zhang, J. Liang, J. Gao, P. D. Walker, and N. Zhang, "Sliding-mode observer based voltage-sensorless model predictive power control of PWM rectifier under unbalanced grid conditions," *IEEE Trans. Ind. Electron.*, vol. 65, no. 7, pp. 5550–5560, Jul. 2018.

[16] Y. Zhang, Z. Wang, J. Jiao, and J. Liu, "Grid-voltage sensorless model predictive control of three-phase PWM rectifier under unbalanced and distorted grid voltages," *IEEE Trans. Power Electron.*, vol. 35, no. 8, pp. 8663–8672, Aug. 2020.

[17] J. Liang, H. Wang, and Z. Yan, "Grid voltage sensorless model-based predictive power control of PWM rectifiers based on sliding mode virtual flux observer," *IEEE Access*, vol. 7, pp. 24007–24016, 2019.

[18] Y. Zhu, M. Cheng, W. Hua, and B. Zhang, "Sensorless control strategy of electrical variable transmission machines for wind energy conversion systems," *IEEE Trans. Magn.*, vol. 49, no. 7, pp. 3383–3386, Jul. 2013.

[19] J. Chen, C. Zhang, X. Xing, and A. Chen, "A fault-tolerant control strategy for T-type three-level rectifier with neutral point voltage balance and loss reduction," *IEEE Trans. Power Electron.*, vol. 35, no. 7, pp. 7492–7505, Jul. 2020.

[20] Y. Wang, H. Li, R. Liu, L. Yang, and X. Wang, "Modulated model-free predictive control with minimum switching losses for PMSM drive system," *IEEE Access*, vol. 8, pp. 20942–20953, 2020.

[21] M. Ahmed, M. Abdelrahem, R. Kennel, and C. M. Hackl, "An enhanced maximum power point tracking based finite-control-set model predictive control for PV systems," in *Proc. 11th Power Electron., Drive Syst., Technol. Conf. (PEDSTC)*, Feb. 2020, pp. 1–6.

[22] Y. Yang, H. Wen, M. Fan, M. Xie, R. Chen, and Y. Wang, "A constant switching frequency model predictive control without weighting factors for T-type single-phase three-level inverters," *IEEE Trans. Ind. Electron.*, vol. 66, no. 7, pp. 5153–5164, Jul. 2019.

[23] S. Bayhan, M. Trabelsi, H. Abu-Rub, and M. Malinowski, "Finite-control-set model-predictive control for a quasi-Z-source four-leg inverter under unbalanced load condition," *IEEE Trans. Ind. Electron.*, vol. 64, no. 4, pp. 2560–2569, Apr. 2017.

[24] P. Acuna, R. P. Aguilera, A. M. Y. M. Ghias, M. Rivera, C. R. Baier, and V. G. Agelidis, "Cascade-free model predictive control for single-phase grid-connected power converters," *IEEE Trans. Ind. Electron.*, vol. 64, no. 1, pp. 285–294, Jan. 2017.

[25] H. Komurcugil, N. Guler, and S. Bayhan, "Weighting factor free Lyapunov-function-based model predictive control strategy for single-phase T-type rectifiers," in *Proc. 46th Annu. Conf. IEEE Ind. Electron. Soc. (IECON)*, Oct. 2020, pp. 4200–4205.

[26] S. Bayhan and H. Abu-Rub, "Performance comparison of two sensorless control methods for standalone doubly-fed induction generator," in *Proc. 16th Int. Power Electron. Motion Control Conf. Expo.*, Sep. 2014, pp. 996–1000.

SERTAC BAYHAN (Senior Member, IEEE) received the bachelor's degree and the M.S. and Ph.D. degrees in electrical engineering from Gazi University, Ankara, Turkey, in 2008 and 2012, respectively. He graduated as valedictorian.

He joined the Electronics and Automation Department, Gazi University, as a Lecturer, in 2008, where he was promoted to an Associate Professor, in 2017. From 2014 to 2018, he worked as an Associate Research Scientist with Texas A&M University, Qatar. He is currently working as a Senior Scientist with the Qatar Environment and Energy Research Institute (QEERI). He is also a Faculty Member with the rank of Associate Professor with the Sustainable Division, College of Science and Engineering, Hamad Bin Khalifa University. He has acquired $13M in research funding and published more than 150 papers in mostly prestigious IEEE journals and conferences. He is the coauthor of two books and five book chapters.

Dr. Bayhan was a recipient of many prestigious international awards, such as the Research Fellow Excellence Award in recognition of his research achievements and exceptional contributions to the Texas A&M University at Qatar, in 2018, the Best Paper Presentation Recognition at the 41st and 42nd Annual Conference of the IEEE Industrial Electronics Society, in 2015 and 2016, the Research Excellence Travel Awards, in 2014 and 2015 (Texas A&M University at Qatar), and the Researcher Support Awards from the Scientific and Technological Research Council of Turkey (TUBITAK). Because of the visibility of his research, he has been recently elected as Chair of IES Power Electronics Technical Committee. He currently serves as an Associate Editor for the IEEE TRANSACTIONS ON INDUSTRIAL ELECTRONICS, the *IEEE Journal of Emerging and Selected Topics in Industrial Electronics*, the *IEEE Open Journal of the Industrial Electronics Society*, and the *IEEE Industrial Electronics Technology News*. He also serves a Guest Editor for the IEEE TRANSACTIONS ON INDUSTRIAL INFORMATICS.